Anatomy of a Catastrophe: Reconstructing the 1936 Rock Fall and Tsunami Event in Lake Lovatnet, Western Norway

Nicolas Waldmann, Kristian Vasskog, Guy Simpson, Emmanuel Chapron, Eivind Wilhelm Nagel Støren, Louise Hansen, Jean-Luc Loizeau, Atle Nesje, Daniel Ariztegui

frontiers in Earth Science

ORIGINAL RESEARCH
published: 28 May 2021
doi: 10.3389/feart.2021.671378

Anatomy of a Catastrophe: Reconstructing the 1936 Rock Fall and Tsunami Event in Lake Lovatnet, Western Norway

Nicolas Waldmann[1]†, Kristian Vasskog[2,3†], Guy Simpson[4], Emmanuel Chapron[5], Eivind Wilhelm Nagel Støren[3,6], Louise Hansen[7], Jean-Luc Loizeau[8], Atle Nesje[6] and Daniel Ariztegui[4]*

[1] Dr. Moses Strauss Department of Marine Geosciences, Charney School of Marine Sciences, University of Haifa, Haifa, Israel, [2] Department of Geography, University of Bergen, Bergen, Norway, [3] Bjerknes Center for Climate Research, University of Bergen, Bergen, Norway, [4] Department of Earth Sciences, University of Geneva, Geneva, Switzerland, [5] Laboratory Geographie De l'Environnement (GEODE), University of Toulouse Jean Jaurès, Toulouse, France, [6] Department of Earth Science, University of Bergen, Bergen, Norway, [7] Geological Survey of Norway, Trondheim, Norway, [8] Department F.-A. Forel for Environmental and Aquatic Science, University of Geneva, Geneva, Switzerland

OPEN ACCESS

Edited by:
Finn Løvholt, Norwegian Geotechnical Institute, Norway

Reviewed by:
Michael Strupler, Swiss Seismological Service, ETH Zurich, Switzerland
Alessandro Romano, Sapienza University of Rome, Italy

***Correspondence:**
Nicolas Waldmann
nwaldmann@univ.haifa.ac.il

† These authors have contributed equally to this work

Specialty section:
This article was submitted to Geohazards and Georisks, a section of the journal Frontiers in Earth Science

Received: *23 February 2021*
Accepted: *26 April 2021*
Published: *28 May 2021*

Citation:
Waldmann N, Vasskog K, Simpson G, Chapron E, Støren EWN, Hansen L, Loizeau J-L, Nesje A and Ariztegui D (2021) Anatomy of a Catastrophe: Reconstructing the 1936 Rock Fall and Tsunami Event in Lake Lovatnet, Western Norway. Front. Earth Sci. 9:671378. doi: 10.3389/feart.2021.671378

Rock falls and landslides plunging into lakes or small reservoirs can result in tsunamis with extreme wave run-ups. The occurrence of these natural hazards in populated areas have encouraged a recent sharp increase of studies that aim to mitigate their impact on human lives and assess infrastructure lost. This paper amalgamates in a novel fashion and at an unprecedented detail *in situ* historic measurements, geological data and numerical modeling of a rock fall event and associated tsunami wave that occurred in Lake Lovatnet (western Norway) in September 1936. Historical records report an event that released ca. 1 million m^3 of rocks and debris from Ramnefjellet Mountain at an altitude of 800 m above Lake Lovatnet. The fragmented material plunged into the lake, causing a tsunami that reached a maximum run-up of 74 m and killed 74 people. In fact, the settlements of Bødal and Nesdal were wiped out as a result of the catastrophic wave. Sediments resulting from the 1936 rock fall and associated tsunami were identified in the subsurface of Lake Lovatnet by shallow geophysical investigations and were retrieved using gravity coring equipment. A set of high resolution physical and geochemical measurements were carried out on the cores with the aim of reproducing a highly detailed reconstruction of this catastrophic event in order to better understand and learn about the processes involved. The cores were retrieved in the northwestern sub-basin of the lake and its chronology was constrained by ^{210}Pb and radiocarbon dating. A specially tailored physically based mathematical model was applied to better understand the tsunami event. Integration of the geophysical record, the sedimentological data and numerical modeling provide a comprehensive background to better understand the effects of such event in a deep fjord-like lacustrine basin and to generate information for better mitigation of similar events elsewhere.

Keywords: mass transport deposits, geohazard, numerical modeling, tsunami deposit, lacustrine sediments, shallow geophysics, cryogenic processes

INTRODUCTION

Subaerial and subaqueous landslides, rock falls and associated sediment mass movements in or near aquatic bodies have been responsible for many tsunamis in high-relief coastal areas around the globe. While these events represent an important landscape-forming factor and serve as major conduits for sediment transport from elevated topography to sedimentary basins, the associated tsunamis pose a considerable hazard to human lives and they have the potential to cause major loss of infrastructure (e.g., Nadim et al., 2006; Shipp et al., 2011; Tanikawa et al., 2014). When the descending masses strike lakes or fjords, the resulting wave activity may last for hours, increasing the hazard and destructiveness (Clague et al., 2003; Pelinovsky, 2006; Harbitz et al., 2014; Mountjoy et al., 2019). In fact, the resulting catastrophic waves occurring in lakes (e.g., Bussmann and Anselmetti, 2010; Kremer et al., 2012, 2015; Gylfadóttir et al., 2017; Leithold et al., 2018) can be comparable to their marine counterparts in terms of both magnitude and strength. A well-documented example for the great ferocity of such hazards is given by the July 9 1958 Lituya Bay tsunami event in Alaska (Fritz, 2001; among others). This event was produced by a magnitude 7.9 earthquake that triggered the detachment of a ca. 5–10 $\times$ 10^6 m^3 subaerial rockslide into a fjord inlet. This generated a tsunami with a maximum run-up height of 524 m, which probably stands as the most prominent event recorded in modern history (Miller, 1960; Lander, 1996).

Mass-movement induced tsunamis occurring in lakes differ from their open ocean counterparts as they (a) affect areas near the wave source, (b) have higher run-ups, (c) strike more rapidly, and (d) pose a greater local hazard, as the degree of confinement of the water body prevents the tsunami energy from escaping, while concurrently inducing stronger and longer seiche (Siegenthaler et al., 1987; Chapron et al., 1999; Schnellmann et al., 2006). Although rock fall- or landslide-generated tsunamis are more localized than those generated by earthquakes (Ruff, 2003), they can produce remarkably high waves, particularly when trapped within small lakes, fjords, semi-enclosed bays or narrow inlets, such as Lituya Bay. Aside from earthquakes, a range of other conditioning factors may trigger landslides or rock falls, including physicochemical deterioration of the substratum by thermal and cryogenic forcing (Draebing et al., 2017), variability in ground humidity (Whiteley et al., 2019) or variability in the precipitation gradients (Hong et al., 2006; Jakob and Lambert, 2009), evaporite dissolution or disintegration of carbonate rocks at depth (Gutiérrez et al., 2008; Benac et al., 2009), biological intervention (Jahn, 1988; Scheidl et al., 2020) and subsurface degassing associated with volcanic complexes (Luckett et al., 2002; Hibert et al., 2011).

Previous studies have shown that the fjords of western Norway are prone to generate major rock falls and landslide events with a magnitude similar to that of Lituya Bay (Furseth, 2006; Jaedicke et al., 2009). In fact, the degree of destruction caused by devastating mass wasting-generated tsunami events in Norwegian fjords and lakes is the highest in the world, as a large percentage of the country's population inhabits the coastline (Hermanns et al., 2014). Although not a tsunami, the largest natural event known to have impacted the population in Norway appears to be the landslide dam burst and associated flood catastrophe that occurred in September 1345 in the Gauldalen valley (**Figure 1A**). Contemporaneous written reports, oral tradition and geological interpretations express divergent opinions about both its exact location and development. However, all agree that the amount of people killed in that disaster was estimated to ca. 500 (Rokoengen et al., 2001). Historical records of tsunami events associated with rock falls include the 1756 Tjellefonna event (Sandøy et al., 2017), the 1934 Tafjord event (Kaldhol and Kolderup, 1936) and the 1905, 1936, and 1950 series of events in Lake Lovatnet (Grimstad, 2006; **Figures 1A,B**). Other identified events in Loen include snow avalanches that destroyed settlements at Breng and Hellsete in 1500 and 1755, respectively, and a series of rock falls that hit settlements at Raudi in 1614 and 1743, with a destructive event on March 2nd 1885 at Kvithammaren (Furseth, 2006; **Figure 1C**). The latter caused the final abandonment of the settlement. Historical records indicate that the fjord region of western Norway has undergone about two to three large-scale catastrophic events every century (Blikra et al., 2006). Thus, for mitigation purposes and in order to study the impact of such an event in generation of possible tsunamis, the Norwegian government has put large efforts during the past decade into studying and monitoring unstable rock slopes such as the Åkneset cliff on the western side of the Sunnylvsfjorden fjord (Sćlevik et al., 2009; **Figure 1B**).

In many aspects, the most notorious and devastating series of rock fall and rock-avalanche events imprinted in modern Norwegian history are those that occurred in Lake Lovatnet. The stained reputation of this site comes from the fact that not one, but a series of events occurred at the same location (Ramnefjellet Mountain; **Figure 1D**), with the most destructive of them occurring in 1905 and 1936 summing a combined death toll of 134 human lives. Despite the numerous events that have struck the fjord area of western Norway, the severity and destructive pattern of these two events coupled with the fact that they occurred at the exact same locality, resulted in a wide-scale repercussion through national broadcasting services, leading to a deeply carved memory in modern Norwegian history.

It is the purpose of the present study to improve the understanding of mechanisms and processes involved in the 1936 rock fall-tsunami event in Lovatnet, through amalgamation of a variety of datasets that include sub-surface imaging, sediment coring and analyses, and numerical modeling based on the shallow water equations. The insight gained here may help to raise awareness concerning similar catastrophes both in Norway and elsewhere in the world.

LAKE LOVATNET

Geological and Hydrological Setting

Lake Lovatnet [ca. 10 km^2 and 52 m above mean sea level (msl)] is a freshwater glacier-fed lake situated in the Lodalen Valley at the head of Nordfjord (**Figures 1B,C**). Given that the local marine limit is at least 80 m above msl (Rye et al., 1997), the Lovatnet basin was part of the fjord for some time following deglaciation.

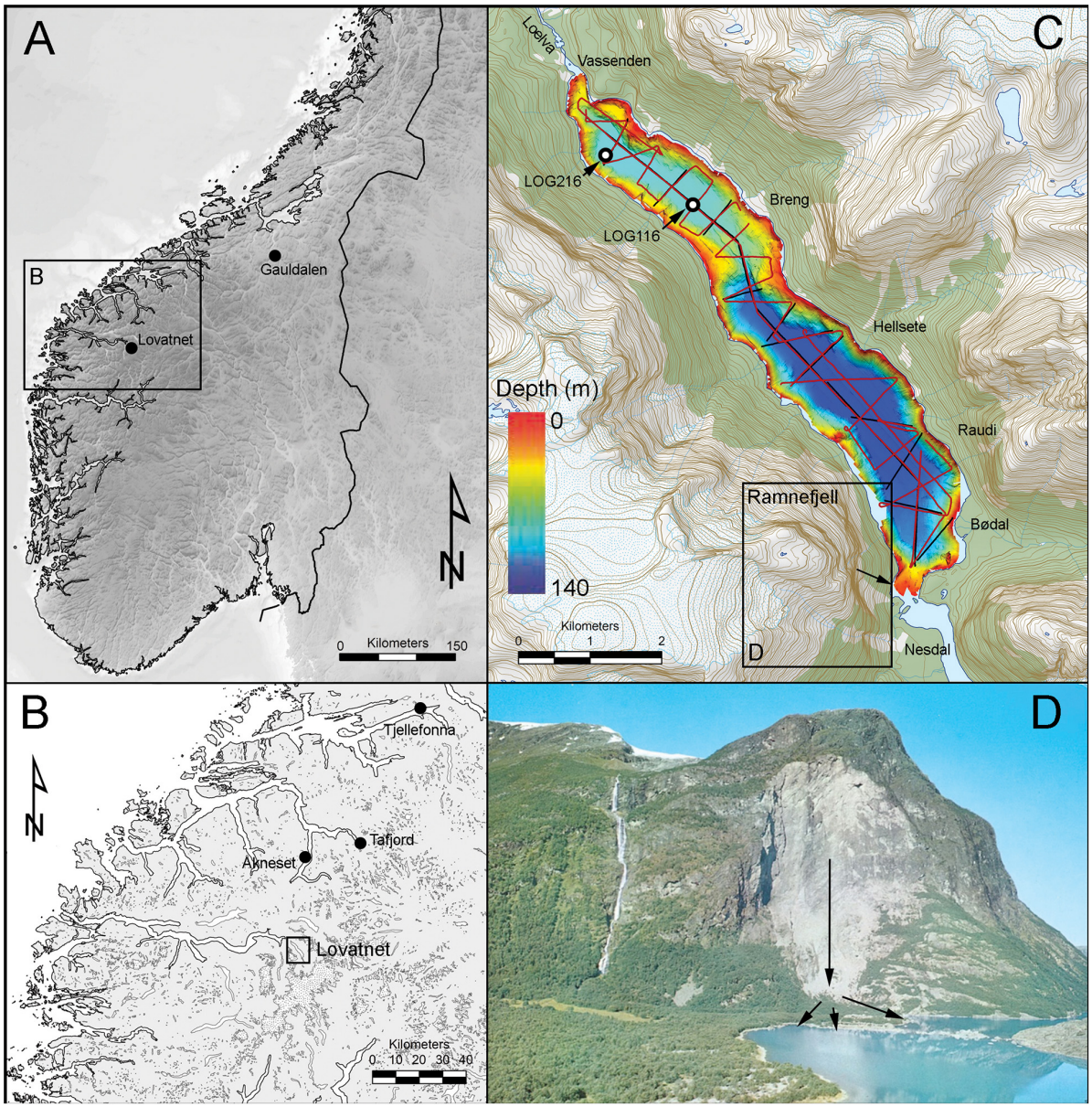

FIGURE 1 | (A) Map of southern Norway, the study area of inner Nordfjord and surrounding region is marked. **(B)** Location of Lake Lovatnet marked by a black square in inner Nordfjord. Sites with known records of rock fall events and associated tsunamis are marked by black dots (see text for more details). **(C)** Swath bathymetric map of Lovatnet showing pinger- (red) and airgun (black) seismic profiles. Sites of cores LOG216 and LOG116 are shown as a white circle in the NW sub-basin. The Ramnefjell slide scar is indicated with an arrow. Lake Lovatnet occupies the entire area of Lodalen Valley. **(D)** Picture of Ramnefjell with the location of the rock fall (Normann, 1963).

The over-deepened character of the basin, with up to 1,000 m high steep valley sides and a typical U-shaped basin floor, was formed by repeated carving of the local glaciers during the Pleistocene glaciations into Cambrian-Silurian schists (e.g., Nesje et al., 1991). The catchment of Lake Lovatnet is 235 km^2 in extent, of which 33% is glaciated, with the lake itself featuring three main river inlets (the Bødalselva, Kjenndalselva and Utigardselva) and a single outlet (Loelva) that drains the lake waters toward Nordfjord. The lake's incoming rivers are fed by three main glaciers: Bødalsbreen, Kjendalsbreen, and Ruteflotbreen, which are all tongues of the major Jostedalsbreen icecap (**Figure 1B**). Previous studies have measured combined sediment and water discharges in the nearby Erdalen valley, pointing to an average of 3.5 m^3/s, with peak flows reaching up to 30 m^3/s (Beylich and Laute, 2015; Beylich et al., 2017).

Previous works using a high-resolution sonar data show that Lake Lovatnet is divided into two sub-basins separated by a morphological high (**Figure 1C**; Hansen et al., 2016). The central

part of the lake floor in each sub-basin is nearly planar, with 90 and 140 m water depth in the northern and southern sub-basins, respectively. Steep marginal slopes rim each sub-basin and are characterized by the total absence of sediments or by a thin sedimentary cover that is directly deposited over the metamorphic bedrock. High-resolution sonar reveals a lake-floor morphology characterized by signs of historic and prehistoric rock falls and landslides (Hansen et al., 2016), pointing to an active source-to-sink lacustrine system with vigorous mass wasting activity. A recent study carried out on a neighboring lake shows that suspended sedimentation with a singular main source (the adjacent glaciers) dominates the limnic depositional system (Storms et al., 2020). Moreover, a study from nearby Lake Oldevatnet shows that the active source-to-sink processes of avalanches and flood activity is more widespread than previously thought, contributing more than 50% of the total lacustrine sedimentation budget at sites located near active avalanche tracks (Vasskog et al., 2011).

The History of Rock Falls in Lake Lovatnet

The event of 1905 happened in the night between January 15th and 16th, when a total volume of 350,000 m^3 of rocks and glacial debris collapsed into the lake from an altitude of ca. 500 m at the eastern side of Mt. Ramnefjellet (Reusch, 1907; Grimstad, 2006). A maximum height of the devastating wave was measured in Nesodden (40.5 m) and reached 14.5 and 15.5 m in the villages of Bødal and Nesdal, respectively (Reusch, 1907; **Figure 2A**). It appears that the tsunami wave wiped clean an entire strip of land along the shoreline of Nesdal and killed 61 from the original population of 122 people (Nesdal, 1983). The wave seiche affected the whole lake reaching a maximum height of 5.8 m at the outlet, which according to historical records caused the destruction of a local bridge over Loelva. A number of subsequent rock falls occurred in the following months, although no lives were lost (Bjerrum and Jørstad, 1968). The mass movement events caused major morphological changes in some parts of the lake. For example, as Sundet (at the southernmost end of the lake), the bathymetry was covered with 5.5 m of debris over an area of ca. 62,500 m^2 (Reusch, 1907). Studies showed that the 1905 rock fall was a consequence of extremely low temperature conditions that caused the water trapped in the sub-vertical joints to freeze and thus to expand and crack, promoting detachment and further collapse of the cliff (Bugge, 1937). Several days after the Loen disaster *Aftenposten* (Norway's largest printed newspaper at the time) chose to use the disaster to make a political statement during a period of constitutional crisis that eventually led to the dissolution of the union with Sweden and creation of the Kingdom of Norway, later in October the same year (Svensen, 2009).

The second event occurred on September 13th 1936, at 5:00 a.m., when a ca. 1 million m^3 block was detached from an altitude of 800 m above Lake Lovatnet, from the same area of Ramnefjellet Mt. (Furseth, 2006; **Figures 1C**, **2B**). The block fragmented and plunged into the lake causing a tsunami wave that reached a maximum run-up of 74 m near the rock-fall site (Jørstad, 1968). The towns of Nesdal and Bødal that were rebuilt after the previous tsunami of 1905 (**Figure 2C**), were again wiped out by the surging catastrophic tsunami wave, leading to a death toll of 74 victims (Hatledal, 2014). In fact, historical records show that only a few houses in the village of Bødal (a dairy and some farm barns) were not affected by the rising waves, probably because they stood further up the hill (Nesdal, 1983). Several verbal narratives were transmitted in local families, such as that of Mr. Anders Bødal, who was 12 years old at the time of the catastrophe. Anders later wrote in a school essay that he was in the garden of his house when he saw the wave arriving over Nesodden. Anders survived, according to his story because he took shelter behind a large rock that protected him, yet the rest of his family members who stayed in the house perished (Hatledal, 2014). The rescue team that was gathered following the 1936 event meticulously mapped the maximum height of the tsunami wave around the entire coastline of Lake Lovatnet (Jørstad, 1968; **Figure 3**) producing an undisputable highly valuable historical documentation of the event that is rarely seen for other sites around the world.

Following the disaster of September 13th, 1936, three additional, smaller landslides were recorded in the same year: (1) on the 21st of September when ca. 10^5 m^3 of rocks fell down and generated a wave that washed up to 40 m in height above the lake; (2) on the 6th of October when an unknown volume of rock fell and generated a wave that sunk several boats; and (3) on the 11th of November with an unregistered volume of rock and no recorded destruction. It is estimated that the total volume of rocks that fell in these three rock fall events was far greater than 1 million m^3 (Grimstad, 2006). The last recorded event occurred on the 22nd of June 1950 at 4:00 p.m., when the crack formed at Mt. Ramnefjellet following the 1936 rock

FIGURE 2 | (A) The settlement of Bødal in CE 1890. **(B)** The Mt. Ramnefjelll slide scar following the 1936 rock fall, with remains of Bødal in the foreground. **(C)** Remains of the settlement Bødal following the rock fall and tsunami event in CE 1936. Following the two events, the settlement was rebuilt 50 m above its past location in order to avoid destruction from a future event. All pictures are from Martinussen and Berg (1937).

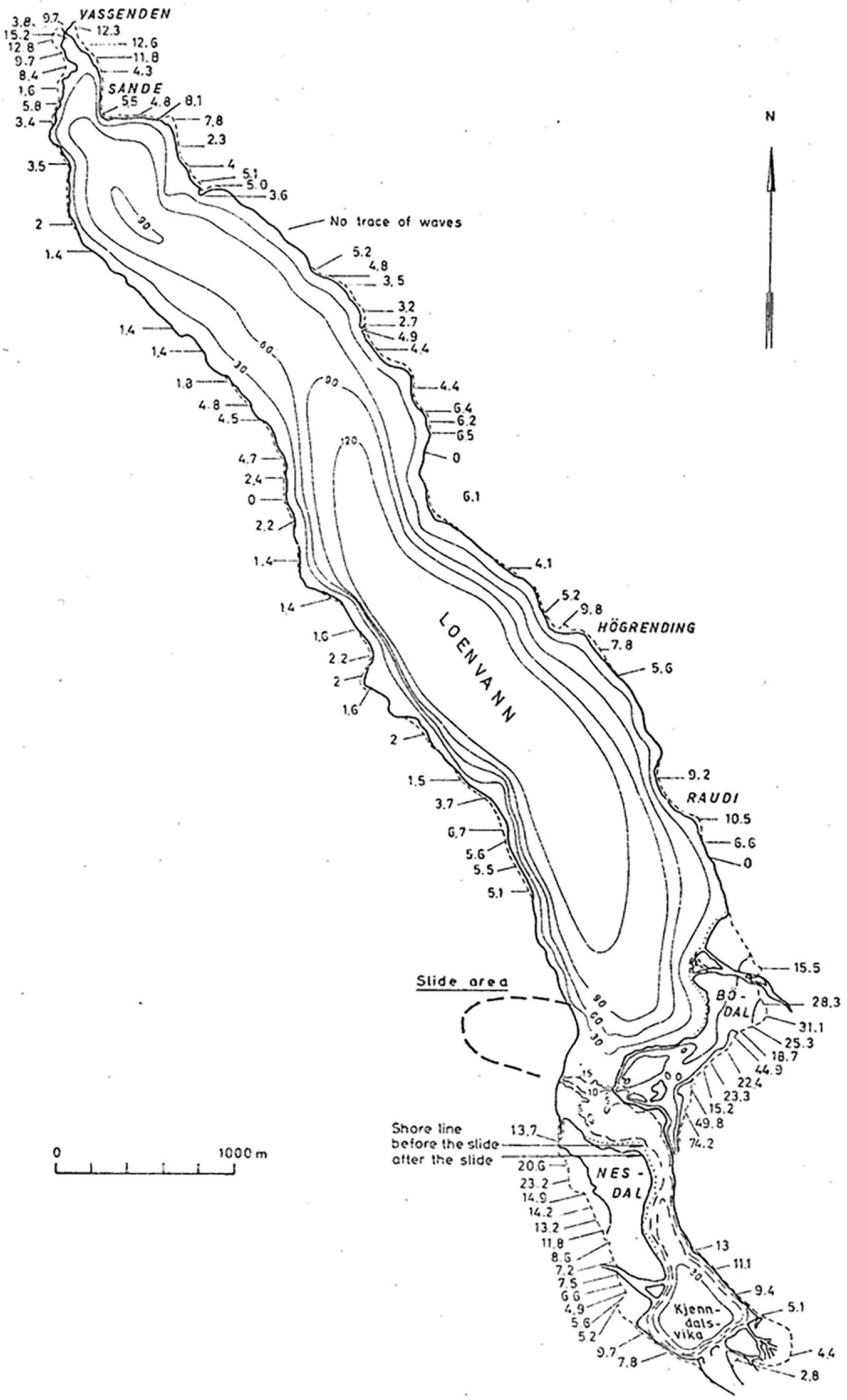

FIGURE 3 | Historical map of Lake Lovatnet with the run-up information measured at high precision following the 1936 tsunami event. Map modified and adapted from Jørstad (1968).

falls expanded and consequently released an estimated volume of ca. 1 million m^3. Considering the shallow water environment below Mt. Ramnefjellet (8–10 m water depth), the wave reached a maximum height of only 15 m (Jørstad, 1954). The settlements of Nesdal and Bødal, which were destroyed twice during the previous events, were built at higher grounds and therefore were situated beyond the wave impact. Historical records show that the 1950 tsunami wave reached a height of 7–8 m at Vassenden at the lake mouth, causing minimal destruction to local infrastructure, including a road and a 30 m long bridge (Jørstad, 1968).

Proposed Triggering Mechanisms for the Lake Lovatnet Rock Falls

During the early Paleozoic Caledonian orogeny, the rocks that are now part of western Norway were intensely deformed, resulting in a series of complex parallel to sub-parallel faults, fractures and lineaments. These features have been continually reactivated through time, and they appear to have played an important role in controlling the location of slope instabilities in more recent times. Equally important with respect to slope instabilities is the Quaternary period during which the region was intensely glaciated, and the steep-sided valleys were formed. As the Scandinavian ice sheet retreated following the last glacial period, the region has undergone significant isostatic uplift, which has provided additional relief along fjords and lakes. Together with the destabilizing effect of glacial debuttressing (e.g., Ballantyne, 2002), this has made the region of western Norway even more susceptible to mass wasting.

The inherited structural framework of the Caledonian orogeny dominates the Ramnefjellet region and has served as an important modulator for slope instabilities and landscape evolution (Redfield and Osmundsen, 2009). A first set of fractures can be followed for several km to the S of the mountain in an often discontinuous fashion, with a spacing ranging between 0.5 and 2 m (Grimstad, 2006). In several cases the vertical protruding fractures run several tens of m below the surface widening toward their tops, from a few cm to > 2 m. A second set of fractures has a NE-SW orientation, a spacing of 0.1 and 0.5 m and dips varying from ca. 35–40° to 22–36° in the northern and southern parts of the fracture, respectively. A less frequent third fracture set can be identified in a vertical direction, almost perpendicular to the mountain side and with a spacing of 30 m to more than 100 m. Historical documents provide valuable information from eyewitnesses during the 1936 event that describe "sudden outbursts of water under high pressure occurring from certain places just above the fractures that delimit the uppermost boundary of the 1905 slide" (Bugge, 1937). Moreover, the documents portray as well "a pulsating water outburst cycle, with each pulse lasting for 1–2 and at 6–7 min intervals." It is estimated that the fractures served as conduits for ground water, which pulsated under increasing high water pressure conditions (Grimstad, 2006). Moreover, it appears that the morphology of the sub-vertical fractures allowed for the storage of large amounts of water during heavy rainfall or snow melting periods, which consequently froze at low temperatures and induced their expansion, further promoting the consequential destabilization of the wall and imminent collapse (**Figure 4**). The rock fall of 1905 provoked the formation of an overhanging shaped edge of ca. 100 m above the bottom of the scar, which consequently fell during the rock fall events of 1936 and 1950 (**Table 1**).

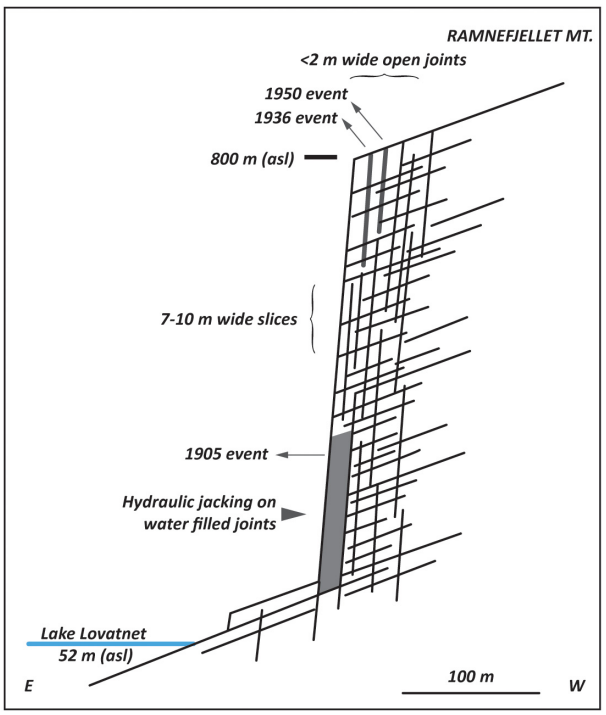

FIGURE 4 | Simplified cross-section across Mt. Ramnefjellet in a W-E direction, describing the general inherited fracture patterns and development of associated series of rock fall events [figure modified from Grimstad (2006)].

APPROACH

In order to better understand the degree of destructiveness associated with a rock fall and accompanying tsunami event in a relatively small but deep lacustrine basin, we carried out a high-resolution study of the event that struck Lake Lovatnet in 1936. A detailed description and analysis of the sedimentary unit (tsunamite) identified in the subsurface of the lake by both shallow geophysical mapping and piston cores was done. Moreover, a description of the processes behind its formation is proposed, while concurrently producing a numerical model of the generated tsunami. The results of this study are framed by historical records hence providing a comprehensive examination of the 1936 rock fall and tsunami event with implications to understand previous events such as the one that occurred in 1905.

Swath Bathymetry

High-resolution bathymetric data was collected in 2005 from Lovatnet using a 125 kHz GeoSwath interferometric side-scan sonar from GeoAcoustics, which was mounted on a locally rented boat. Data was collected at a speed around 4 knots and with a general line spacing of 100 m. Sound velocity profiles (SVP) were measured using a Valeport 650 SVP. Water level during the survey was measured digitally using a submerged Valeport 740 instrument. A base station was used for a positioning on dm-scale (RTK) and a gyroscope was used to adjust navigation. In locations with poor signal coverage, primarily due to the high relief, a differential GPS was used for positioning, giving a horizontal accuracy of ±1 m. The accuracy of depth measurements during data acquisition was on dm-scale. Processing was conducted using the GeoSwath software and included sound velocity correction and calibration to reduce

TABLE 1 | List of historical rock fall events occurring in the Lovatnet Valley (Jørstad, 1968).

Date	Total volume (m^3)	Height of the rock fall (m above lake)	Maximum measured wave height (m)	Lives lost
15/01/1905	350,000	500	40.5	61
20/09/1905	∼15,000	400	>15	0
13/09/1936	∼100,000	800	74.2	74
21/09/1936	1 million	800	∼40	0
6/10/1936	?	800	?	0
11/11/1936	> 1 million	800	>74	0
22/6/1950	∼1 million	800	∼15	0

signal-to-noise ratios. Merging of data and calculation of a 1 m grid was also carried out in the GeoSwath software.

Seismic Survey

The seismic survey was carried out in summer of 2006, simultaneously combining a multi-channel airgun (Sercel) and a single channel high-resolution 3.5 kHz pinger profiling system (Geoacoustic), both attached to a local trawler boat (to the stern and port side, respectively, navigation grid shown in **Figure 1C**).

The deployed airgun used a dominant frequency of 400 Hz and a nominal pressure of 80 bar, with data recorded using a 12-channel streamer (1 hydrophone per channel), a 24-bit seismograph (Geometrics Strataview), and positioned by an onboard GPS with an average accuracy of ± 5 m. The survey was conducted with an average constant boat speed of ca. 4 knots, allowing the airgun to fire at 5 m horizontal intervals under the control of a computer-driven triggering system that adjusts the firing rate according to the boat's velocity (Pugin et al., 1999). Receiver, shot, and offset spacing were all 7 m, which yielded a nominal sixfold data coverage and a nominal common depth-point (CDP) spacing of 3.5 m. Following acquisition, processing of the data was carried out utilizing the open system Seismic Unix utility (developed by CWP) and considering parameters as described in Beres et al. (2008).

For the pinger system, an Octopus acquisition unit was used for imaging the obtained seismic signal on board and for later processing. The pinger data was band-pass filtered (2–6 kHz) and gained with an Automated Gain Control (AGC; 100 ms). For both airgun and pinger data, seismic profiles were digitally recorded in SEG-Y format, and a water bottom mute was applied with constant shallow noise digitally removed. Acoustic velocities of 1,470 and 1,500 m/s were assumed for the water column and the sedimentary infill, respectively. All seismic data was interpreted using Kingdom Suite software packages, developed by Information Handling Services (IHS, Inc.).

Core Retrieval, Sedimentology, and Chronology

Based on the seismic data interpretation, two gravity cores were retrieved (LOG116 and LOG216) from Lake Lovatnet in autumn of 2016 utilizing an Uwitec gravity corer (**Figure 1C**). Both cores were retrieved from the NW sub-basin utilizing a rigid aluminum raft supported by two inflatable Zodiac boats. Core LOG116 was obtained at water depths of 89 m near the main depocenter and core LOG216 was retrieved more distal to the rock fall area and closer to the western shore at water depths of 92.5 m (see location in **Figures 1C**, 5B). Following fieldwork, the cores were transported to the University of Bergen to be stored under 4°C in dark conditions. The cores were analyzed at the University of Bergen EARTHLAB laboratory facilities, where they were first cut lengthwise into halves, photographed, and visually described in detail, prior to carrying out further analytical measurements. One of the core halves was stored for future reference (archive halves), while the other (working halves) was scanned with a Geotek^{TM} multi-sensor core logger (MSCL) to obtain gamma-ray attenuation (γ-ray) density and surface magnetic susceptibility (MS), and an ITRAX core scanner (Croudace et al., 2006) to obtain geochemical X-Ray Fluorescence (XRF) data. XRF measurements were performed at 500 μm (LOG116) and 200 μm resolution (LOG216) using a molybdenum X-ray source at 30 kV and 50 mA for an exposure time of 10 s. Geotek measurements were performed with a downcore resolution of 0.5 cm in LOG116 and 0.2 cm in LOG216.

In order to determine sediment accumulation rates in the recent sedimentary sequence, natural and artificial radionuclides (^{241}Am, ^{210}Pb, and ^{137}Cs) were measured at the Department F.-A. Forel for Environmental and Aquatic Science, University of Geneva (Switzerland). The samples were subsampled from core LOG116 every half cm down to 10.5 cm depth and every cm between 45.5 and 54.5 cm. Each sample was weighed, freeze-dried and weighed again to measure water content and ensure a dry weight between 2 and 5 g (minimum weight 2.75 g, maximum 4.99 g). ^{137}Cs, ^{210}Pb, and ^{241}Am activity profiles were obtained using a HPGe well gamma spectrometer (Ortec EG&G) measuring gamma emissions at 46.5 and 662 keV. Prior to ^{210}Pb analysis, samples were sealed in a glass tube to prevent any loss of ^{222}Rn and stored for a period of 3 weeks to ensure secular equilibrium between ^{226}Ra and ^{214}Pb. Excess ^{210}Pb was calculated as the difference between total ^{210}Pb and the supported ^{210}Pb determined by ^{214}Pb measurement (Appleby, 2001). The detection efficiency was corrected for geometry and density using Monte Carlo simulation software (Gespecor 4.1, Sima et al., 2001). ^{210}Pb ages were calculated considering the Constant Rate of Supply model (CRS, Appleby, 2001). Sediment accumulation rates (g cm^{-2} y^{-1}) were calculated using sediment bulk dry density (Sanchez-Cabeza and Ruiz-Fernández, 2012). The radioactive fallouts from nuclear weapon tests in the atmosphere and from the Chernobyl accident were used as markers to test the ^{210}Pb chronological model (Appleby, 2001).

A single sample of terrestrial plant macrofossils was extracted from a depth of 77.5–80 cm depth in core LOG216, in order to constrain the full age range covered by the cores. The sample (Poz-93757) was submitted to the Poznan Radiocarbon Laboratory (Poland) for AMS radiocarbon dating, and calibrated in OxCal using the IntCal20 atmospheric calibration curve (Reimer et al., 2020).

Tsunami Modeling

We modeled the wave propagation associated with the 1936 rock fall in Lake Lovatnet using the shallow water equations in two dimensions (Simpson and Castelltort, 2006). The paleo-bathymetry for the model was estimated by interpreting high resolution seismic profiles. Modeling the processes involved when a rock fall enters a lake is a complex task that requires different specific tools, such as full 3D CFD techniques (e.g., Chen et al., 2020; Romano et al., 2020; Rauter et al., 2021) or 2D-3D experimental models (Fritz et al., 2004; Evers et al., 2019), both not presently used as our study is based on a simpler and less computationally demanding approach. Here we treat only the movement of an assumed known volume of material within the lake, while we neglect effects related to the impact of the slide mass on the surface. Thus, our models are expected to significantly underestimate wave heights. We also treat the edge of the lake as a solid boundary, which does not permit us to compute inundation and run-up distances, as done by others (Lindstrøm et al., 2014; Heller and Spinneken, 2015; Løvholt et al., 2015a,b; Bellotti and Romano, 2017). This solid boundary approximation might be a reasonable along steep portions of the lake, but it will tend to exaggerate boundary reflections relative to a model that treats run-up correctly. Reflected edge waves tend to be dispersive and are expected to slow the lateral propagation of the wave. Nevertheless, we expect our model to provide a reasonable first order estimate of lateral propagation of the first wave across the lake.

The wave in our models was generated by instant adding of a mass of sediments and rocks to the base of the lake, thus locally modifying the bathymetry near the rock fall. Please note that we did not treat the impact of the slide mass on the surface of the lake, since this would require a more complicated 3d model. The area and volume of the mass movement were constrained from historical data, but we considered a range of volumes from 10^5 to 10^7 m^3. The mass movement is initiated in the lake at the base of Mt. Ramnefjellet where the water depth is currently 122 m. The velocity at which the rock mass moves within the lake was computed using a simple empirical relationship (Ward and Day, 2002):

$$v = (gL_c sin(\alpha)/8)^{\frac{1}{2}}$$

where L_c is the slide length and α is the initial angle of the slide surface.

This relationship is certainly a strong simplification of the complex processes involved in subaqueous mass-movements as it tends to overestimate the velocity, ignores frictional deceleration and neglects the influence of the possible contribution of additional dislocated sediments as a consequence of seiche waves (Thorpe, 1998). Nevertheless, it provides a first order estimate of the slide velocity and its dependence on mean slope angle and run out distance.

RESULTS

Bathymetric Data

The floor of Lake Lovatnet displays several debris lobes from failures along the lateral slopes (Hansen et al., 2016), with the most prominent identified around the area between Ramnefjellet and Nesodden (**Figure 5A**). The whole deposit appears to extend ca. 1.8 km northwards, including ca. 1 km along the basin floor plain. Here, two major debris lobes make up a total volume of at least 1.2×10^6 m^3 (Hansen et al., 2016). Some debris are also present along the lateral slopes to the west and near Bødalsdelta to the east (**Figure 5A**). In the area of the lake's outlet, furrows appear at the bottom that can be followed from the Vassenden area into the deep basin. Here, minor lobes occupy the basin floor, and an array of small debris mounds can be followed far into the lake (**Figure 5B**). The distance from Vassenden to the southernmost tip of the debris is ca. 1.5 km. One of the southernmost debris mounds includes a 15 m long and 1 m high feature, which could potentially be the remains of the vessel Lodølen that disappeared during the 1936 event (Hansen et al., 2016).

Seismic Reflection Data

The airgun survey provided excellent imaging of the deeper units, including the bedrock morphology, while the pinger survey offered seismic stratigraphic information of the shallow subsurface sediments (up to a depth of ca. 10 m). Based on the seismic stratigraphy analysis of the airgun data acquired in Lake Lovatnet, six seismic units were identified: LOV-S1 to LOV-S6, from bottom to top, respectively (**Figure 6A**). At 250 ms [two-way travel time (TWTT)] seismic energy faded and prevented good visualization of possible deeper substratum units. Unit LOV-S1 is characterized by chaotic and discontinuous internal refractions, bounded on top by discontinuous high-amplitude shattered reflections with a prominent rough surface of irregular morphology. The overlying LOV-S2 unit can be occasionally identified as discontinuous internal strong refractions that onlap the top of LOV-S1 in a clear truncation. The unit is not prominent and was identified only on scattered areas of the basin. Seismic units LOV-S3 to LOV-S6 show a much clearer internal morphology, and indicate the initiation of a different sedimentation pattern, probably pointing to a limnic-(or glacio-marine)-style basin infill. LOV-S3 is characterized by semi-transparent to transparent facies with occasional medium-energy parallel discontinuous internal semi-parallel to parallel reflections. The overlying seismic unit LOV-S4 shows continuous internal reflections occasionally changing spatially to more chaotic closer to the central promontory that divides the basin into two sub-basins. The LOV-S5 unit, however, is chaotic with significant lateral thickness variations that ponds toward the deeper basin depocenter. The topmost seismic unit LOV-S6 drapes all previous units and consists of very clear and strong

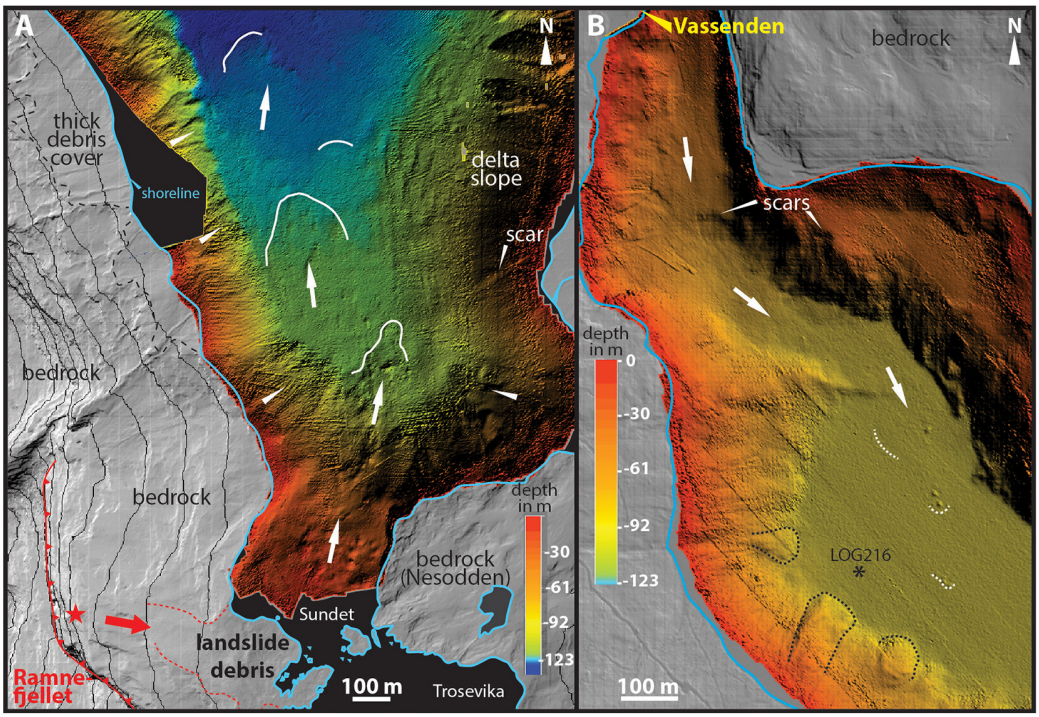

FIGURE 5 | Detailed shaded-relief images from the southern and northern ends of Lake Lovatnet. The images are based on high resolution topographical data from LiDAR and high-resolution swath bathymetry (modified from Hansen et al., 2016). **(A)** The escarpment at Ramnefjellet is highlighted in red. The path of landslide debris from the rock-slope and into the lake is shown by the large white arrows, with the front of distinct interpreted MTD lobes shown in white lines. Additional debris was entrained from the lateral slopes (small white arrows). **(B)** The northern part of Lovatnet displays an array of minor lobes and debris. North of the array are furrows that can be followed to shallow water near Vassenden. Location of core LOG216 is marked.

continuous reflections that intercalate with low-amplitude to transparent ponded intervals, which greatly increase in thickness toward the deeper parts of the basin. Seismic units LOV-S5 and S6 are clearly identified in the pinger seismic profiles (**Figures 6B,C,F**), where a great increase in thicknesses (up to 10 m) is revealed in the central parts of both sub-basins. In this areas, LOV-S6 includes internal sub-units characterized by stacked, chaotic and transparent seismic facies divided by clear strongly undulated and rough reflectors (**Figures 6B–F**). At least five of these stacked chaotic and semi-transparent sub-units are well identified and named LOV-S6a to LOV-S6f, although more of these units can also locally be recognized. Some of such intervals locally increase in their thicknesses (e.g., LOV-S6e, **Figures 6D,E**), which might reflect contribution from local processes.

Sedimentological Data

Both cores LOG116 and LOG216 show a very similar lithostratigraphic pattern, with alternating dark and light gray laminae, occasionally disturbed by thicker dark brown units of variable thickness topped by light gray mud caps (**Figure 7**). Three main sedimentary facies were recognized in core LOG116 and LOG216, here numbered as Facies I–III:

- **Facies I** consists of a light gray, laminated, highly minerogenic, clayey silt, interpreted to reflect the continuous "background" pelagic-type sedimentation in Lovatnet. As about one third of Lake Lovatnet's catchment is covered by glaciers, a large part of the background sedimentation may thus come from contemporaneous glacier erosion. However, a significant part may also be derived from re-mobilization of different kinds of unconsolidated materials in the catchment, such as till or colluvium. Some of the lamina are several mm in thickness, and might be related to episodic sedimentation events.
- **Facies II** appear as dark gray to brown layers, ranging in thickness from 1 to 3 cm. The dark, brownish color is due to high organic content, mainly in the form of plant macrofossils, although in some cases the organic detritus can be very fine, similar to gyttja. Most of the facies II layers contain coarser minerogenic grains than the background sediments, either scattered in a matrix of organic material or as massive sand layers that are usually overlain by more organic-rich layers. Facies II layers are interpreted as Mass Transport Deposits (MTDs) resulting from (snow-) avalanches, flood events, and sub-aquatic slope processes, similar to what was found in nearby Lake Oldevatnet (Vasskog et al., 2011). In core LOG216 some of the facies II deposits are capped by a light gray layer of clayey silt.
- **Facies III** represents a more complex sedimentary succession found between 43.5 and 10.5 cm depth in core LOG116 and 28–9 cm in core LOG-216, and has

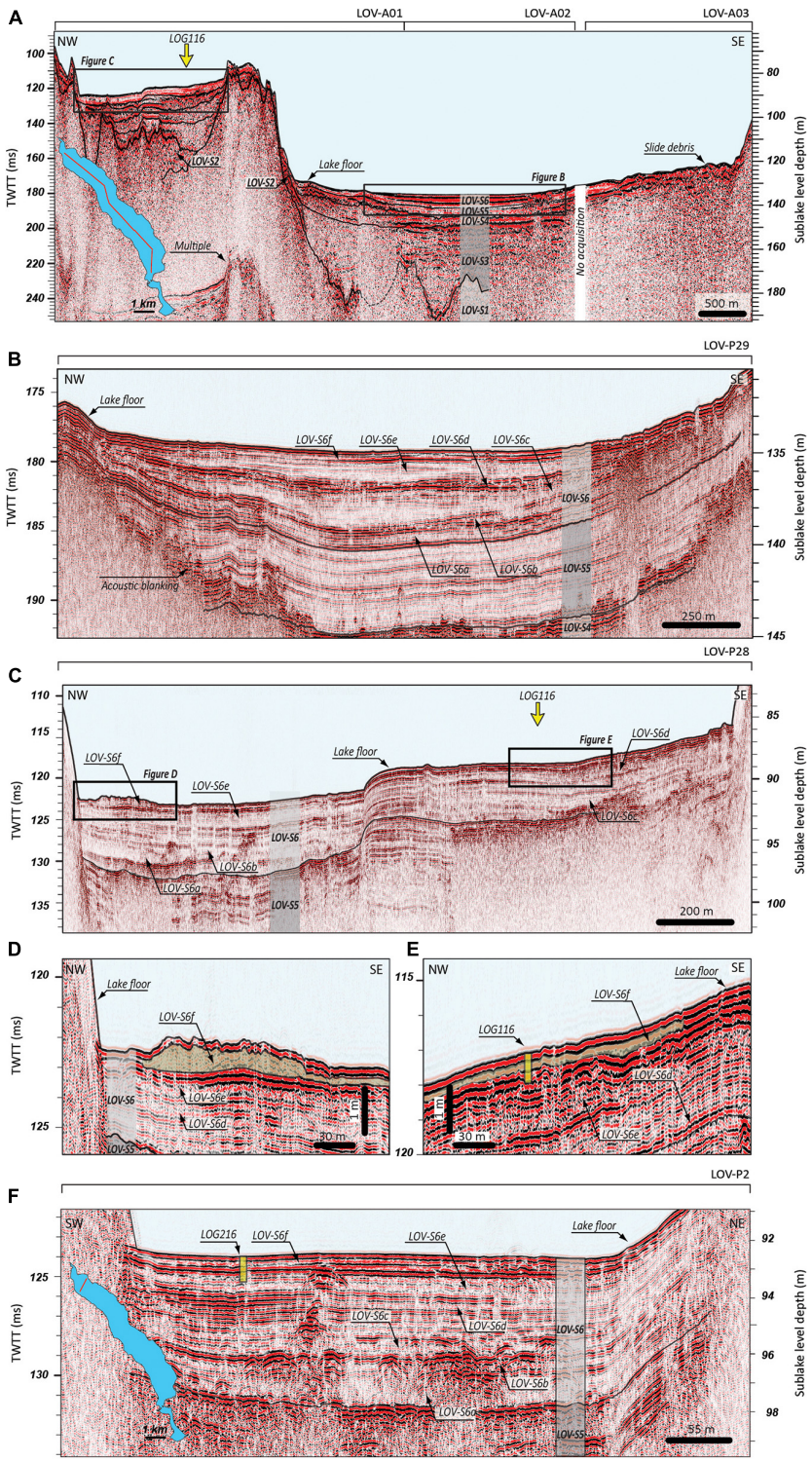

FIGURE 6 | (A) Longitudinal airgun seismic profile across the lake axis (NW-SE). Location of the airgun line is marked in the map. **(B)** Pinger profile P29 across the SE sub-basin, with location marked in **(A)** by a black square. Internal stacked sub-units are marked (LOV-S6a to LOV-S6f) and stands for a series of rock falls and debris flows (see discussion for more detail). **(C)** Pinger profile in the shallow sub-basin (location in **A**). **(D)** Zoomed area in **(C)** near the lake's outlet highlighting the local increase in thickness of LOV-S6f, probably as a result of the seiche effect and local contribution to the debris. **(E)** Zoomed area in the location of the cores retrieved in the lake, with highlight of LOV-S6f. **(F)** Pinger profile P2 across the NW sub-basin, location marked in the inlet figure. Location of core LOG216 is marked, as well as the stacked subunits of LOV-S6 (LOV-S6a to LOV-S6f).

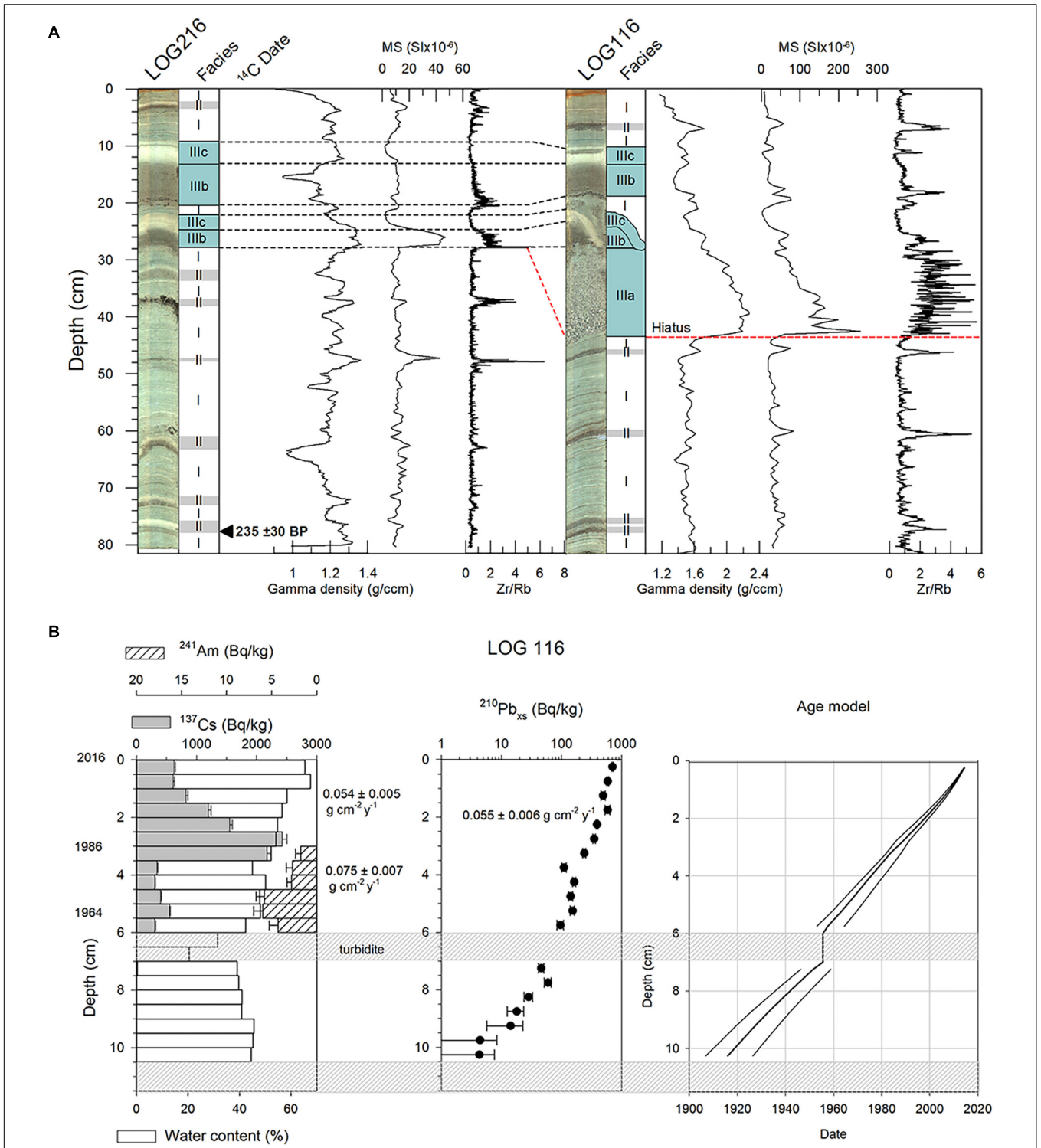

FIGURE 7 | (A) Photographs of LOG216 (left) and LOG116 (right) with corresponding measurements of gamma ray density, Magnetic Susceptibility (MS), and Zr/Rb-ratios from the XRF scanning. **(B)** Age-depth model for the upper section of LOG116 based on ^{137}Cs, ^{210}Pb, and ^{241}Am.

therefore been divided into three sub-facies (**Figure 7**). **Facies IIIa** is only found in LOG-116, and comprises a normally graded unit that is fining upwards from very fine gravel (2.5 mm) at the base to medium sand in the top. The overlying **facies IIIb** features a dark brown layer of concentrated plant macrofossils in the base, overlain by a lighter brown, organic-rich silt with a high content of small plant macrofossils throughout. The uppermost **facies IIIc** consists of a light, clayey silt. Facies III is interpreted as a more complex MTD than facies II. Two repeating sequences of facies IIIb–IIIc is recognized in both cores, separated by a 3–5 cm section of facies I. This facies I-section, together with the lowermost facies IIIc layer, is strongly deformed in core LOG116, probably due to disturbance during coring.

Facies II and III layers, here interpreted as episodic sedimentation events or MTDs, are well captured by the MS and XRF data (**Figure 7A**) with particularly distinct spikes seen in the Zr/Rb ratio. This ratio is thought to reflect grain-size, as resistant Zr minerals are typically enriched in coarser grain-sizes and consequently known to peak in turbidites (Rothwell et al., 2006).

A radiocarbon age of 235 ± 30 a BP was obtained for the sample at 78–77.5 cm depth in LOG216 (Poz-93757), which produced multiple modes of possible ages after calibration due to large fluctuations in the calibration curve over the last few hundred years (Reimer et al., 2020). The two most likely calibrated age ranges returned at a 95% confidence level were 1634–1684 CE (48.4% likelihood) and 1735–1804 CE (39.7% likelihood). Broadly speaking, this indicates that the LOG216 core covers the period from somewhere between 1634 and 1804 CE until present, and by lithostratigraphic correlation LOG116 should cover a similar age range. Thus, the radiocarbon dating indicates that the sedimentary signals of the historical rock fall and tsunami events of 1905, 1936, and 1950 should be captured within the retrieved cores. Using the average facies-I bulk dry density measured in LOG116 (0.84 g cm^{-3}), and the most likely age range of the radiocarbon date (1634–1684 CE), an average dry Sediment Accumulation Rate (SAR) of 0.11 ± 0.01 g cm^{-2} y^{-1} can be calculated for LOG216 background sedimentation (facies I).

An age model based on ^{210}Pb indicates an average SAR of 0.055 ± 0.006 g cm^{-2} y^{-1} for the upper 6 cm of LOG116, and 0.04 ± 0.011 g cm^{-2} y^{-1} between 7 and 10.5 cm, i.e., below the facies II layer at 6–7 cm (marked as turbidite in **Figure 7B**). The measured ^{137}Cs-content in the uppermost sediments shows two spikes at 2.75 and 5.25 cm, which are inferred to reflect fallout from the Chernobyl accident (1986 CE) and peak nuclear bomb testing (1964 CE), respectively. A corresponding peak in ^{241}Am at 5.25 cm supports the inferred age of 1964 CE for this depth. From this, the artificial radionuclides agree well with the ^{210}Pb model in the upper 2.75 cm of LOG116, where they indicate a SAR of 0.054 ± 0.005 g cm^{-2} y^{-1}. Below this level, however, they deviate, with ^{137}Cs and ^{241}Am suggesting a SAR of 0.075 ± 0.007 g cm^{-2} y^{-1} for the period between the Chernobyl accident and peak nuclear fallout. **Figure 7B** shows an age model based on the artificial radionuclide tie-points between 0 and 6 cm, and extrapolation of the same SAR further downwards to 10.5 cm. With these assumptions, the model indicates an approximate age of 1956 (1951–1962) CE for the facies II layer at 6–7 cm depth and an age of 1914 (1904–1924) CE for the facies III succession below 10.5 cm.

Simulation of the 1936 Tsunami Event

As stated in section "Tsunami Modeling," the simplicity of our numerical model does not permit to compute run-up distances or realistic wave amplitudes. However, our model is of use to estimating how the first wave spreads across the lake with time. Our models show that lateral propagation of the wave is mainly controlled by the geometry and bathymetry of the lake, both of which are quite well constrained with geophysics. In such a small mass of water, wave arrival times are extremely short, often on the order of minutes for sites located close to the initiation site. In Lake Lovatnet, the most distal sites appear to have received the first wave after a little more than 10 min (**Figure 8**). This estimate is consistent with eyewitness accounts of the Tsunami.

DISCUSSION

The primary objective of the current contribution is to study the sedimentary imprint and model the rock fall and associated tsunami wave that occurred in Lake Lovatnet in September 1936. The amalgamation of geophysical imaging (pinger), with results obtained from the sediment cores and framed by a robust chronology, allows us to model the impact of the 1936 tsunami and to correlate with the historical records.

Seismic Interpretation

The qualitative construction of an event stratigraphy record based on our pinger sub-bottom profiler is constrained by some limiting factors, which needs to be taken into account. This includes both external elements (such as the nature of the slide and resulting sedimentary facies) and internal elements (such as decisions taken during retrieval of the seismic data). While some of these factors were partially addressed during processing of the seismic data, others such as the vertical resolution of a specific event layer (dm scale) or the survey grid density (few hundred m), impede detection of very thin and/or spatially limited MTDs. Thus, a record of MTDs based solely on subsurface geophysical imaging may lack several types of events, such as those that left a limited sedimentary imprint on the lake bottom or those with the same lithology as the surrounding pelagic environment. Moreover, the density of the seismic grid influences the mapping and volume calculations of the identified MTDs (Clare et al., 2018). Possible improvements include a densification of the dataset and post-processing of high-quality seismic data, such as the one acquired by 3D sub-bottom profiler (Vardy et al., 2017). Moreover, a secondary component that needs to be taken into account is the low signal-to-noise ratio and signal masking in deeper parts of the sedimentary infill due to the gradual decrease of transmitted (and reflected) seismic energy with depth and the potential presence of gas-rich levels. These two depth-related

factors have a major effect in the calculated amount of MTDs in the lower parts of the seismic profiles.

The lithology produced at the lake floor as a consequence of the rock fall event may also generate some restrictions when producing a rigorous stratigraphy. For instance, increase in grain size may impede proper imaging of the unit boundaries and prevent the acoustic signal to penetrate the layer (Girardclos et al., 2007). Moreover, the presence of repeated events can lead to the generation of stacked MTDs with unclear boundaries (e.g., Lindhorst et al., 2016), which is especially true in case of erosive events that impede the proper separation of each generated unit. In those cases, the proper identification is carried out on the distal part of the basin, where the units are typically non-erosive and bear fewer fluid escape features. The last factor which needs to be considered is the operator prejudice in the assignment of stratigraphic levels and identification of MTDs. In several cases, the interpretation of the seismic profiles leads to grouping some MTDs on a single level, whereas in reality they may relate to closely spaced levels. Such bias is difficult to account for, but may be reduced by allowing different persons to interpret the data or by a standardized protocol (e.g., Oswald et al., 2021).

In Lake Lovatnet, the signal penetration is restricted to only few dm beneath the lake floor in the areas near Ramnefjell where the rock fall originated (**Figure 6A**), probably as a result of the local presence of slide debris composed of coarser material, which inhibit the acoustic signal to return a clear image of the subsurface. Moreover, the seismic architecture of unit LOV-6S is characterized by a series of irregular stacked MTDs across the whole deep part of the SE basin (**Figure 6B**), which in turn complicates any attempt to properly identify and separate each single event. We identify six MTDs in the deeper LOV-S6 sequence (sub-units LOV-S6a to LOV-S6f), which should be considered a minimum estimate, as some events might have been missed and left unidentified due to methodological restrictions. Nevertheless, we propose that sub-unit LOV-S6f corresponds to the 1936 tsunami event, as it is estimated by merging our seismic interpretation with the information retrieved from the two cores and their respective chronologies. Unfortunately, an accurate volume calculation for sub-unit LOV-S6f (and thus for the 1936 event) could not be generated. This exercise might have led to misinterpretations as disentangling between the 1905 and 1936 events in the seismic data is below the resolution of the acquisition system. Yet, our event stratigraphy model proposes that the 1936 catastrophe might have not been the sole to occur in Lake Lovatnet that has left a meaningful impact in the deep lacustrine environment, yet we do not have the sufficient information to propose their chronologies or triggering mechanisms.

Chronological and Sedimentological Interpretations

We have analyzed two short gravity cores from Lake Lovatnet (LOG116 and LOG216) to investigate whether the major rock fall and tsunami event of 1936 CE left a distinguishable sedimentary imprint in the lake deposits. Dating results from ^{137}Cs and ^{241}Am were only in agreement with ^{210}Pb down to a depth of 2.75 cm in LOG116, after which they deviate, with the artificial radionuclides suggesting an increasing SAR with depth and ^{210}Pb suggesting the opposite. Here, we have chosen to rely more on

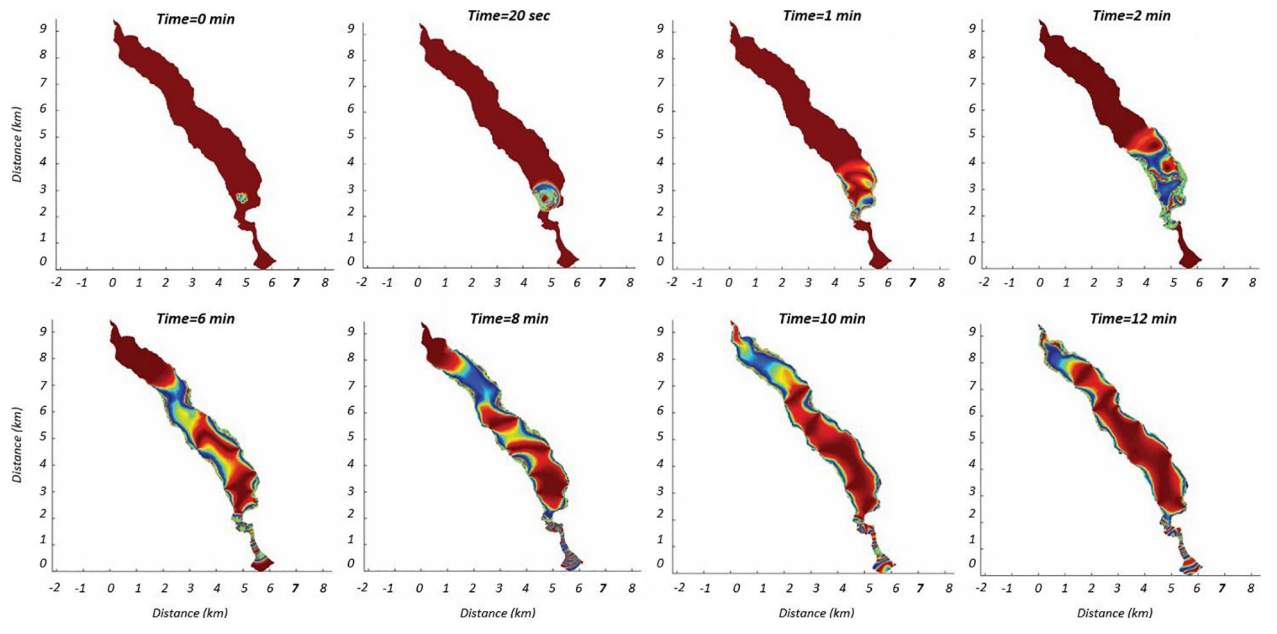

FIGURE 8 | Maps of Lake Lovatnet showing the result of the numerical model reconstruction of the 1936 tsunami waves caused by the rock fall at different modeled times (time = zero). The model corroborates historical records conserving the time that passed since the first tsunami wave was generated until it reached the other extreme of the lake (10 min). Please note that the vertical scale of the tsunami is not shown on purpose, since the model is too simplified to provide an accurate prediction.

the artificial radionuclides, because an increasing SAR with depth seems most reasonable. This argument is based on the regional glacier history, which indicates that glacial activity and associated erosion and delivery of glacio-fluvial sediment to Lake Lovatnet should increase as we move back in time toward the local "Little Ice Age" period (Vasskog et al., 2012). A detailed reconstruction of the Briksdalsbreen glacier in the neighboring Oldedalen Valley shows a distinct retreat phase between 1934 and 1950 CE (Nesje, 2005), and it is reasonable to believe that the glaciers draining into Lake Lovatnet followed a similar pattern, although with small variations based on different response times of individual glaciers. The SAR indicated by artificial radionuclides at depths of 2.75–5.25 cm (0.075 ± 0.007 g cm^{-2} y^{-1}) is also approaching the overall SAR for the entire LOG216 core based on radiocarbon dating (0.11 ± 0.01 g cm^{-2} y^{-1}), further supporting the idea of an increasing SAR downcore. As we no longer have tie-points from artificial radionuclides below 7 cm, our extrapolated age model (**Figure 7B**) might still overestimate the age of the facies III layer at 10.5 cm at 1904–1924 CE, given the probability of a further increasing SAR. If we employ the most likely radiocarbon-based SAR in the extrapolation, however, we obtain an age of 1939–1923 CE for the upper facies-III succession in LOG116. This allows for the possibility that this succession was deposited by the historical 1936 CE rock fall and tsunami event, and we will further argue that this is the case based on sedimentological evidence.

Clearly, episodic MTDs form an important part of Lake Lovatnet's sedimentation budget, with facies II and III making up almost half of the sediments contained in LOG116 and LOG216. Facies III layers are distinguished from facies II layers because they are thicker and have a clear internal succession of sub-facies, in addition to the fact that the facies IIIb and IIIc-layers appear near identical in the two cores, which are separated by a distance of 1.6 km. Tentative correlations can be made between some of the smaller facies-II layers, but they do not appear identical in both cores, and are therefore more likely to represent locally sourced MTDs, possibly from (snow-) avalanches, floods and subaqueous slope failures. The events that deposited the two repeating successions of facies IIIb–IIIc must, on the other hand, have affected the entire northern sub-basin of Lake Lovatnet in a similar manner during emplacement of these MTDs, which together with the thickness of these deposits suggest events of a considerable magnitude. Facies IIIa is only identified in the lower succession of LOG116, which suggests the contribution of local sources at this site during this event. Normally graded sand layers similar to that of facies IIIa are common units following tsunami events with contributing material sourced from the coastal areas that are hit by the wave (Dawson and Shi, 2000). Similar layers have been previously identified in several lake settings in western Norway and correlated with the Storegga tsunami (Bondevik et al., 1997b; Vasskog et al., 2013). Similarly, facies IIIb might be analogous to the organic detritus found in deposits from the Storegga tsunami, termed facies 7 by Bondevik et al. (1997a), which also represent material washed into the lake from onshore areas. Facies IIIc (light gray mud capping the sequence) has been attributed to suspension fallout following subaqueous density flows (Mulder and Alexander, 2001), but have also been correlated with seiche effects following tsunami events (e.g., Waldmann et al., 2011; Vasskog et al., 2013; Kempf et al., 2015; Nigg et al., 2021). Based on the above points, we suggest that the facies III successions represent major tsunami events that affected the whole lake basin. While the reasons facies IIIa only occurs within the lowermost event are still unclear, we postulate that these sediments originated from a local source (e.g., exposed sandy glacio-fluvial deposits), which might have not been present when the latter event occurred.

To summarize: we interpret the facies III succession found at 43–25 cm and 28–22 cm in cores LOG116 and LOG216, respectively, as deposits from the 1905 CE rock fall and tsunami, whereas the succession found at 20–10.5 cm and 20–9 cm in cores LOG116 and LOG216, respectively, to correspond to the 1936 rock fall and tsunami. As far as we know, the 1905 and 1936 events are unparalleled in magnitude over the period covered by our sediment cores, and from the sedimentological evidence it therefore seems likely that these two prominent facies III successions indeed reflect the historical events. While the chronology of the cores is not sufficiently precise to pinpoint the exact age of these deposits, it places them roughly within the correct age bracket, thereby strengthening our sedimentological interpretation.

Modeling the Tsunami of 30 September 1936

Determination of arrival times modeled for the Lake Lovatnet 1936 tsunami is critically important for proposing early warnings, for planning evacuation efforts, and for mitigation avenues. Moreover, these calculations serve as example for prevention of similar catastrophes in comparable lacustrine basins elsewhere in the world. The arrival times are determined by wave celerity, which in case of a linear wave propagation velocity is controlled by the wave-length and the water depth, taking into consideration a linear dispersion relation (Mohammed and Fritz, 2012). In the present numerical model, while the first and second basin-wide waves fall into a linear regime, the near field waves are non-linear due to the very shallow depth of the water (few meters) and the extreme volume of the added rock mass (1 M m^3). Moreover, it should be considered that individual crests and troughs of the rock fall-generated tsunami wave have independent wavelengths and propagate with different velocities. Interestingly, despite the limitations of our model, results show that the arrival time of the first wave generated by the 1936 tsunami event to the lake's outlet happened 10 min after its initial generation by the rock fall (**Figure 8**). This suggests a mean linear wave velocity of 13.3 m s^{-1}, which is in concordance with previous observations elsewhere (Truong, 2012) and taking into consideration the confined, deep and narrow basin that characterizes Lake Lovatnet. The arrival time of the first wave at different sites in the lake shoreline seems to be in good concordance with historical records (Bugge, 1937). Together, these results imply that early warning is extremely challenging in small water bodies. Although the current model does not address the impact of the tsunami wave and associated seiche on the lake surroundings, we believe that our model results could be merged with the historical record

(**Figure 3**) and produce a more complex 3D fluid dynamics model as a potential topic for future studies.

SUMMARY AND CONCLUSION

In the current study, we present a wide spectrum of information that includes geological, geophysical, and historical datasets concerning the 1936 rock fall and associated tsunami event that occurred in Lake Lovatnet. The following points summarize our study:

- A series of rock fall events associated with tsunamis occurred in Lake Lovatnet (inner Nordfjord region, western Norway) in 1905, 1936, and 1950, with the first two events being catastrophic and causing a combined loss of 134 human lives.
- A high-resolution shallow geophysical survey (pinger) was carried out in the lake aiming to identify the imprint of the 1936 event in the sedimentary infill. Meticulous seismic stratigraphy analysis allows to identify a series of units down to tens of dm in thickness, which are interpreted as MTDs. Among these units, two appear to correspond to the 1905 and 1936 rock fall and tsunami events.
- Based on high resolution seismic stratigraphy interpretation, two gravity cores (LOG216 and LOG116) were retrieved in the shallower NW sub-basin of the lake aiming to penetrate these MTD units. The cores lithology shows intercalations of alternating dark and light gray laminae, in which events layers are occasionally identified as thicker dark brown units topped by light gray mud caps (interpreted to results from the seiche effect following the tsunamis).
- The cores were logged for geochemistry and petrophysics and subsequently sampled for constraining their chronology through amalgamation of radiocarbon and radionuclides measurements (^{137}Cs and ^{210}Pb). Only through the combination of these dating techniques, were we able to constrain the ages of the MTD events identified in the cores and to provide explanations for the processes that were involved in their formation.
- A numerical model was produced combining the geophysical and historical data in order to reproduce the tsunami generated by the 30 of September 1936 rock fall. Our model, based on the shallow water equations, shows that the size and magnitude of the 1936 event is comparable to similar events that have occurred in other similar settings. Thus, our study provides valuable data that help to better understand the mechanisms and processes involved in rock fall-tsunami events. Finally, we expect that the current study will provide valuable information that in the long perspective, might help to raise the awareness and mitigate similar catastrophes both in western Norway and elsewhere in the world.
- The current study provides valuable information concerning the relative short time the tsunami wave generated during the 1936 rock fall traveled the whole length of the lake (10 min). This information is in concordance with measurements carried out in similar settings elsewhere and enlighten with valuable information on how to mitigate for possible generation of similar geohazards in Norway and in worldwide similar settings.

DATA AVAILABILITY STATEMENT

The original contributions presented in the study are included in the article/**Supplementary Material**, further inquiries can be directed to the corresponding author/s.

AUTHOR CONTRIBUTIONS

NW, EC, AN, and DA participated in fieldwork, gathered the data, and conceived of the presented idea. KV collected the sediment cores. NW and KV contributed equally to the writing of the manuscript with partial support of DA. J-LL performed the chronological analyses. GS developed the theory and performed the computations and modeling. LH contributed with the multibeam map of the lake. Sediment cores were analyzed by KV and ES. All authors discussed the results and contributed to the final manuscript.

FUNDING

KV was partly funded by the EISCLIM project (Research Council of Norway, Grant No. 229788). All sediment core analyses were done at the EARTHLAB National Infrastructure (Grant No. NRC 226171), University of Bergen. This work was supported by the Swiss National Science Foundation (Grant Nos. 200021-100668/1 and 200020-111928/1 to DA).

ACKNOWLEDGMENTS

We would like to thank Jostein Bakke (University of Bergen, Norway), Laura Sanna (Consiglio Nazionale delle Ricerche, Italy), Flavio Anselmetti (University of Bern, Switzerland), and Richard Gyllencreutz (Stockholm University, Sweden) for the invaluable help they provided in the field, lab and for many long and fruitful scientific discussions. We thank IHS for granting academic licenses for Kingdom Suite (universities of Geneva and Haifa).

SUPPLEMENTARY MATERIAL

The Supplementary Material for this article can be found online at: https://www.frontiersin.org/articles/10.3389/feart.2021.671378/full#supplementary-material

Supplementary Movie 1 | Moving visual simulation of the 1936 tsunami event.

REFERENCES

Appleby, P. G. (2001). "Chronostratigraphic techniques in recent sediments," in *Tracking Environmental Change Using Lake Sediments. Volume I: Basin Analysis, Coring, and Chronological Techniques*, eds W. M. Last and J.-P. Smol (Dordrecht: Kluwer Academic Publishers), 171–203. doi: 10.1007/0-306-47669-X_9

Ballantyne, C. (2002). Paraglacial geomorphology. *Q. Sci. Rev.* 21, 1935–2017. doi: 10.1016/S0277-3791(02)00005-7

Bellotti, G., and Romano, A. (2017). Wavenumber-frequency analysis of landslide-generated tsunamis at a conical island. Part II: EOF and modal analysis. *Coast. Eng.* 128, 84–91. doi: 10.1016/j.coastaleng.2017.07.008

Benac, È, Dugonjić, S., Arbanas, Ž, Oštrić, M., and Jurak, V. (2009). "The origin of instability phenomena along the karst-flysch contacts," in *ISRM International Symposium Rock Engineering in Difficult Ground Conditions: Soft Rock and Karst*, ed. I. Vrkljan (Cavtat: CRC Press), 757–761.

Beres, M., Gilli, A., Ariztegui, D., and Anselmetti, F. S. (2008). The Lago Cardiel Basin, Argentina (49 S): origin and evolution revealed by high-resolution multichannel seismic reflection studies. *J. South Am. Earth Sci.* 25, 74–85. doi: 10.1016/j.jsames.2007.08.001

Beylich, A. A., and Laute, K. (2015). Sediment sources, spatiotemporal variability and rates of fluvial bedload transport in glacier-connected steep mountain valleys in western Norway (Erdalen and Bødalen drainage basins). *Geomorphology* 228, 552–567. doi: 10.1016/j.geomorph.2014.10.018

Beylich, A. A., Laute, K., and Storms, J. E. (2017). Contemporary suspended sediment dynamics within two partly glacierized mountain drainage basins in western Norway (Erdalen and Bødalen, inner Nordfjord). *Geomorphology* 287, 126–143. doi: 10.1016/j.geomorph.2015.12.013

Bjerrum, I., and Jørstad, F. (1968). *Stability of Natural Rock Slopes in Norway*, Tech. Rep. 79. Oslo: Norwegian Geotechnical Institute (NGI).

Blikra, L., Longva, O., Braathen, A., Anda, E., Dehls, J., and Stalsberg, K. (2006). *Rock Slope Failures in Norwegian Fjord Areas: Examples, Spatial Distribution and Temporal Pattern, Landslides From Massive Rock Slope Failure*. Berlin: Springer, 475–496. doi: 10.1007/978-1-4020-4037-5_26

Bondevik, S., Svendsen, J. I., and Mangerud, J. (1997a). Tsunami sedimentary facies deposited by the Storegga tsunami in shallow marine basins and coastal lakes, western Norway. *Sedimentology* 44, 1115–1131. doi: 10.1046/j.1365-3091.1997.d01-63.x

Bondevik, S., Svendsen, J. I., Johnsen, G., Mangerud, J., and Kaland, P. E. (1997b). The Storegga tsunami along the Norwegian coast, its age and runup. *Boreas* 26, 29–53. doi: 10.1111/j.1502-3885.1997.tb00649.x

Bugge, A. (1937). Fjellskred fra topografisk og geologisk synspunkt. *Norsk Geogr. Tidssk.* 6, 342–360. doi: 10.1080/00291953608551553

Bussmann, F., and Anselmetti, F. S. (2010). Rossberg landslide history and flood chronology as recorded in Lake Lauerz sediments (Central Switzerland). *Swiss J. Geosci.* 103, 43–59. doi: 10.1007/s00015-010-0001-9

Chapron, E., Beck, C., Pourchet, M., and Deconinck, J.-F. (1999). 1822 earthquake-triggered homogenite in Lake Le Bourget (NW Alps). *Terra Nova* 11, 86–92. doi: 10.1046/j.1365-3121.1999.00230.x

Chen, F., Heller, V., and Briganti, R. (2020). Numerical modelling of tsunamis generated by iceberg calving validated with large-scale laboratory experiments. *Adv. Water Resour.* 142:103647. doi: 10.1016/j.advwatres.2020.103647

Clague, J. J., Munro, A., and Murty, T. (2003). Tsunami hazard and risk in Canada. *Nat. Hazards* 28, 435–463. doi: 10.1023/A:1022994411319

Clare, M. A., Le Bas, T., Price, D. M., Hunt, J. E., Sear, D., Cartigny, M. J., et al. (2018). Complex and cascading triggering of submarine landslides and turbidity currents at volcanic islands revealed from integration of high-resolution onshore and offshore surveys. *Front. Earth Sci.* 6:223. doi: 10.3389/feart.2018.00223

Croudace, I. W., Rindby, A., and Rothwell, R. G. (2006). ITRAX: description and evaluation of a new multi-function X-ray core scanner. *Geol. Soc. Lond. Spec. Publ.* 267, 51–63. doi: 10.1144/GSL.SP.2006.267.01.04

Dawson, A. G., and Shi, S. (2000). Tsunami deposits. *Pure Appl. Geophys.* 157, 875–897. doi: 10.1007/s000240050010

Draebing, D., Krautblatter, M., and Hoffmann, T. (2017). Thermo−cryogenic controls of fracture kinematics in permafrost rockwalls. *Geophys. Res. Lett.* 44, 3535–3544. doi: 10.1002/2016GL072050

Evers, F., Heller, V., Fuchs, H., Hager, W. H., and Boes, R. (2019). Landslide-generated Impulse waves in reservoirs: basics and computation. *VAW Mitteil.* 11:254.

Fritz, H. M. (2001). Lituya Bay case rockslide impact and wave run-up. *Sci. Tsun. Hazards* 19, 3–22.

Fritz, H. M., Hager, W. H., and Minor, H.-E. (2004). Near field characteristics of landslide generated impulse waves. *J. Water. Port Coast. Ocean Eng.* 130, 287–302. doi: 10.1061/(ASCE)0733-950X(2004)130:6(287)

Furseth, A. (2006). *Skredulykker i Norge*. Oslo: Tun Forlag, 207.

Girardclos, S., Schmidt, O. T., Sturm, M., Ariztegui, D., Pugin, A., and Anselmetti, F. S. (2007). The 1996 AD delta collapse and large turbidite in Lake Brienz. *Mar. Geol.* 241, 137–154. doi: 10.1016/j.margeo.2007.03.011

Grimstad, E. (2006). "The Loen rock slide-an analysis of the stability," in *Proceedings of the 11th International Conference and Field Trip on Landslides, Norway, September 2005: Landslides and Avalanches*, eds K. Senneset, K. Flaate, and J. O. Larsen (London: Taylor & Francis).

Gutiérrez, F., Calaforra, J., Cardona, F., Ortí, F., Durán, J., and Garay, P. (2008). Geological and environmental implications of the evaporite karst in Spain. *Environ. Geol.* 53, 951–965. doi: 10.1007/s00254-007-0721-y

Gylfadóttir, S. S., Kim, J., Helgason, J. K., Brynjólfsson, S., Höskuldsson, Á, Jóhannesson, T., et al. (2017). The 2014 Lake Askja rockslide-induced tsunami: optimization of numerical tsunami model using observed data. *J. Geophys. Res. Oceans* 122, 4110–4122. doi: 10.1002/2016JC012496

Hansen, L., Waldmann, N., Storms, J. E. A., Eilertsen, R. S., Ariztegui, D., Chapron, E., et al. (2016). Morphological signatures of mass wasting and delta processes in a fjord-lake system: insights from Lovatnet, western Norway. *Norweg. J. Geol.* 96, 9–29. doi: 10.17850/njg96-3-02

Harbitz, C. B., Glimsdal, S., Løvholt, F., Kveldsvik, V., Pedersen, G. K., and Jensen, A. (2014). Rockslide tsunamis in complex fjords: from an unstable rock slope at Åkerneset to tsunami risk in western Norway. *Coast. Eng.* 88, 101–122. doi: 10.1016/j.coastaleng.2014.02.003

Hatledal, E.-M. (2014). *Raset frå Ramnefjell: Reaksjonar og Tiltak Etter Lodalsulykka i 1936, Department of Archaeology, Conservation and History*. M. Sc. dissertation. Oslo: University of Oslo.

Heller, V., and Spinneken, J. (2015). On the effect of the water body geometry on landslide–tsunamis: Physical insight from laboratory tests and 2D to 3D wave parameter transformation. *Coast. Eng.* 104, 113–134. doi: 10.1016/j.coastaleng.2015.06.006

Hermanns, R. L., Oppikofer, T., Roberts, N. J., and Sandøy, G. (2014). *Catalogue of Historical Displacement Waves and Landslide-Triggered Tsunamis in Norway, Engineering Geology for Society and Territory*, Vol. 4. Berlin: Springer, 63–66. doi: 10.1007/978-3-319-08660-6_13

Hibert, C., Mangeney, A., Grandjean, G., and Shapiro, N. (2011). Slope instabilities in Dolomieu crater, Réunion Island: From seismic signals to rockfall characteristics. *J. Geophys. Res. Earth Surf.* 116:F04032. doi: 10.1029/2011JF002038

Hong, Y., Adler, R., and Huffman, G. (2006). Evaluation of the potential of NASA multi-satellite precipitation analysis in global landslide hazard assessment. *Geophys. Res. Lett.* 33:8010. doi: 10.1029/2006GL028010

Jaedicke, C., Lied, K., and Kronholm, K. (2009). Integrated database for rapid mass movements in Norway. *Nat. Hazards Earth Syst. Sci.* 9, 469–479. doi: 10.5194/nhess-9-469-2009

Jahn, J. (1988). "Deforestation and rockfall," in *Proceedings of the International Congress, Interpraevent*, Graz, 185–198.

Jakob, M., and Lambert, S. (2009). Climate change effects on landslides along the southwest coast of British Columbia. *Geomorphology* 107, 275–284. doi: 10.1016/j.geomorph.2008.12.009

Jørstad, F. A. (1954). *Beretning over Norges Geotekniske Institutts Virksomhet fra 1. Januar 1954 til 31. Desember 1955, NGI-Report*. Oslo: Norges Geotekniske Institutts.

Jørstad, F. A. (1968). *Waves Generated by Landslides in Norwegian Fjords and Lakes*. Oslo: Norwegian Geotechnical Institute Publication, 22.

Kaldhol, H., and Kolderup, N.-H. (1936). *Skredet i Tafjord 7. april 1934. Bergens Museums Årbok 1936 Naturvitenskapelig Rekke*, Vol. 11. Bergen: Bergens Museum, 1–15.

Kempf, P., Moernaut, J., Van Daele, M., Vermassen, F., Vandoorne, W., Pino, M., et al. (2015). The sedimentary record of the 1960 tsunami in two coastal

lakes on Isla de Chiloé, south central Chile. *Sedimen. Geol.* 328, 73–86. doi: 10.1016/j.sedgeo.2015.08.004

Kremer, K., Hilbe, M., Simpson, G., Decrouy, L., Wildi, W., and Girardclos, S. (2015). Reconstructing 4000 years of mass movement and tsunami history in a deep peri-Alpine lake (Lake Geneva, France-Switzerland). *Sedimentology* 62, 1305–1327. doi: 10.1111/sed.12190

Kremer, K., Simpson, G., and Girardclos, S. (2012). Giant Lake Geneva tsunami in AD 563. *Nat. Geosci.* 5, 756–757. doi: 10.1038/ngeo1618

Lander, J. F. (1996). *Tsunamis Affecting Alaska, 1737-1996*. Boulder, CO: National Geophysical Data Center, 196.

Leithold, E. L., Wegmann, K. W., Bohnenstiehl, D. R., Smith, S. G., Noren, A., and O'Grady, R. (2018). Slope failures within and upstream of Lake Quinault, Washington, as uneven responses to Holocene earthquakes along the Cascadia subduction zone. *Q. Res.* 89:178. doi: 10.1017/qua.2017.96

Lindhorst, K., Krastel, S., and Baumgarten, H. (2016). *Mass Wasting History Within Lake Ohrid Basin (Albania/Macedonia) Over the Last 600 ka, Submarine Mass Movements and their Consequences*. Berlin: Springer, 291–300. doi: 10.1007/978-3-319-20979-1_29

Lindstrøm, E. K., Pedersen, G. K., Jensen, A., and Glimsdal, S. (2014). Experiments on slide generated waves in a 1: 500 scale fjord model. *Coast. Eng.* 92, 12–23. doi: 10.1016/j.coastaleng.2014.06.010

Løvholt, F., Glimsdal, S., Lynett, P., and Pedersen, G. (2015a). Simulating tsunami propagation in fjords with long-wave models. *Nat. Hazard. Earth Syst. Sci.* 15, 657–669. doi: 10.5194/nhess-15-657-2015

Løvholt, F., Pedersen, G., Harbitz, C. B., Glimsdal, S., and Kim, J. (2015b). On the characteristics of landslide tsunamis. *Philos. Transact. R. Soc. A Math. Phys. Eng. Sci.* 373:20140376. doi: 10.1098/rsta.2014.0376

Luckett, R., Baptie, B., and Neuberg, J. (2002). The relationship between degassing and rockfall signals at Soufriere Hills Volcano, Montserrat. *Geol. Soc. Lond. Mem.* 21, 595–602. doi: 10.1144/GSL.MEM.2002.021.01.28

Martinussen, H., and Berg, F. G. S. (1937). *Naturkatastrofer i Norge, Nasjonalbiblioteket Digital 2009-09-21*. Bergen: Nasjonalbiblioteket.

Miller, D. J. (1960). Giant waves in Lituya Bay, Alaska. *Bull. Seismol. Soc. Am.* 50, 253–266. doi: 10.3133/pp354C

Mohammed, F., and Fritz, H. M. (2012). Physical modeling of tsunamis generated by three-dimensional deformable granular landslides. *J. Geophys. Res. Oceans* 117:7850. doi: 10.1029/2011JC007850

Mountjoy, J. J., Wang, X., Woelz, S., Fitzsimons, S., Howarth, J. D., Orpin, A. R., et al. (2019). "Tsunami hazard from lacustrine mass wasting in Lake Tekapo, New Zealand," in *Subaqueous Mass Movements and their Consequences: Assessing Geohazards, Environmental Implications and Economic Significance of Subaqueous Landslides*, eds D. G. Lintern, D. C. Mosher, L. G. Moscardelli, P. T. Bobrowsky, C. Campbell, J. D. Chaytor, et al. (London: The Geological Society of London), 413–426. doi: 10.1144/SP477.21

Mulder, T., and Alexander, J. (2001). The physical character of subaqueous sedimentary density flows and their deposits. *Sedimentology* 48, 269–299. doi: 10.1046/j.1365-3091.2001.00360.x

Nadim, F., Kjekstad, O., Peduzzi, P., Herold, C., and Jaedicke, C. (2006). Global landslide and avalanche hotspots. *Landslides* 3, 159–173. doi: 10.1007/s10346-006-0036-1

Nesdal, S. (1983). *Lodalen, Fager og Fårleg*. Tønsberg: Ekspresstrykk, 125.

Nesje, A. (2005). Briksdalsbreen in western Norway: AD 1900-2004 frontal fluctuations as a combined effect of variations in winter precipitation and summer temperature. *Holocene* 15, 1245–1252. doi: 10.1191/0959683605hl897rr

Nesje, A., Kvamme, M., Rye, N., and Løvlie, R. (1991). Holocene glacial and climate history of the Jostedalsbreen region, Western Norway; evidence from lake sediments and terrestrial deposits. *Q. Sci. Rev.* 10, 87–114. doi: 10.1016/0277-3791(91)90032-P

Nigg, V., Wohlwend, S., Hilbe, M., Bellwald, B., Fabbri, S. C., de Souza, G. F., et al. (2021). A tsunamigenic delta collapse and its associated tsunami deposits in and around Lake Sils, Switzerland. *Nat. Hazards* 21, 1–15. doi: 10.1007/s11069-021-04533-y

Normann (1963). *Ramnefjellet på Austsida av Lodalsvatnet*. Stryn Municipality: Fylkesarkivet i Sogn og Fjordane.

Oswald, P., Strasser, M., Hammerl, C., and Moernaut, J. (2021). Seismic control of large prehistoric rockslides in the Eastern Alps. *Nat. Commun.* 12:1059. doi: 10.1038/s41467-021-21327-9

Pelinovsky, E. (2006). "Hydrodynamics of tsunami waves," in *Waves in Geophysical Fluids. CISM International Centre for Mechanical Sciences*, eds J. Grue and K. Trulsen (Vienna: Springer).

Pugin, A., Pullan, S. E., Burns, R., Douma, M., and Good, R. (1999). "High-resolution, multichannel, marine seismic surveying using a small airgun source," in *Proceedings of the 12th EEGS Symposium on the Application of Geophysics to Engineering and Environmental Problems*, (Houten: European Association of Geoscientists & Engineers). doi: 10.3997/2214-4609-pdb.202.1999_028

Rauter, M., Hoße, L., Mulligan, R. P., Take, W., and Løvholt, F. (2021). Numerical simulation of impulse wave generation by idealized landslides with OpenFOAM. *Coast. Eng.* 165:103815. doi: 10.1016/j.coastaleng.2020.103815

Redfield, T., and Osmundsen, P. (2009). The Tjellefonna fault system of Western Norway: linking late-Caledonian extension, post-Caledonian normal faulting, and Tertiary rock column uplift with the landslide-generated tsunami event of 1756. *Tectonophysics* 474, 106–123. doi: 10.1016/j.tecto.2009.02.006

Reimer, P. J., Austin, W. E., Bard, E., Bayliss, A., Blackwell, P. G., Ramsey, C. B., et al. (2020). The IntCal20 Northern Hemisphere radiocarbon age calibration curve (0–55 cal kBP). *Radiocarbon* 62, 725–757. doi: 10.1017/RDC.2020.41

Reusch, H. (1907). Skredet i Loen 15 de januar 1905. Norges geologiske undersøkelse. *Aarbok* 1907, 3.

Rokoengen, K., Jespersen, M. N., Kleiv, R. A., and Sćterbø, E. (2001). The 1345 slide and flood disaster in the Gauldalen valley, Mid-Norway: a new interpretation. *Norsk Geograf. Tidsskr.* 55, 57–70. doi: 10.1080/00291950121138

Romano, A., Lara, J., Barajas, G., Di Paolo, B., Bellotti, G., Di Risio, M., et al. (2020). Tsunamis generated by submerged landslides: numerical analysis of the near-field wave characteristics. *J. Geophys. Res. Oceans* 125:e2020JC016157. doi: 10.1029/2020JC016157

Rothwell, R. G., Hoogakker, B., Thomson, J., Croudace, I. W., and Frenz, M. (2006). Turbidite emplacement on the southern Balearic Abyssal Plain (western Mediterranean Sea) during Marine Isotope Stages 1–3: an application of ITRAX XRF scanning of sediment cores to lithostratigraphic analysis. *Geol. Soc. Lond. Spec. Publ.* 267, 79–98. doi: 10.1144/GSL.SP.2006.267.01.06

Ruff, L. (2003). *Some Aspects of Energy balance and tsunami generation by earthquakes and landslides, Landslide Tsunamis: Recent Findings and Research Directions*. Berlin: Springer, 2155–2176. doi: 10.1007/978-3-0348-7995-8_18

Rye, N., Nesje, A., Lien, R., Blikra, L. H., Eikenaes, O., Hole, P., et al. (1997). Glacial geology and deglaciation chronology of the area between inner Nordfjord and Jostedalsbreen Strynefjellet, western Norway. *Norsk Geol. Tidsskr.* 77, 51–63.

Sćlevik, G., Jensen, A., and Pedersen, G. (2009). Experimental investigation of impact generated tsunami; related to a potential rock slide, Western Norway. *Coast. Eng.* 56, 897–906. doi: 10.1016/j.coastaleng.2009.04.007

Sanchez-Cabeza, J., and Ruiz-Fernández, A. (2012). 210Pb sediment radiochronology: an integrated formulation and classification of dating models. *Geochim. Cosmochim. Acta* 82, 183–200. doi: 10.1016/j.gca.2010.12.024

Sandøy, G., Oppikofer, T., and Nilsen, B. (2017). Why did the 1756 Tjellefonna rockslide occur? A back-analysis of the largest historic rockslide in Norway. *Geomorphology* 289, 78–95. doi: 10.1016/j.geomorph.2016.08.016

Scheidl, C., Heiser, M., Vospernik, S., Lauss, E., Perzl, F., Kofler, A., et al. (2020). Assessing the protective role of alpine forests against rockfall at regional scale. *Eur. J. For. Res.* 20, 1–12.

Schnellmann, M., Anselmetti, F. S., Giardini, D., and Mckenzie, J. A. (2006). 15,000 Years of mass-movement history in Lake Lucerne: implications for seismic and tsunami hazards. *Eclo. Geol. Helvet.* 99, 409–428. doi: 10.1007/s00015-006-1196-7

Shipp, R. C., Weimer, P., and Posamentier, H. W. (2011). *Mass-Transport Deposits in Deepwater Settings*. Tulsa, OK: SEPM Soc for Sed Geology. doi: 10.2110/sepmsp.096

Siegenthaler, C., Finger, W., Kelts, K., and Wang, S. (1987). Earthquake and seiche deposits in Lake Lucerne, Switzerland. *Eclo. Geol. Helvet.* 80, 241–260.

Sima, O., Arnold, D., and Dovlete, C. (2001). GESPECOR: a versatile tool in gamma-ray spectrometry. *J. Radioanal. Nuclear Chem.* 248, 359–364. doi: 10.1023/A:1010619806898

Simpson, G., and Castelltort, S. (2006). Coupled model of surface water flow, sediment transport and morphological evolution. *Comput. Geosci.* 32, 1600–1614. doi: 10.1016/j.cageo.2006.02.020

Storms, J. E., Beylich, A. A., Hansen, L., and Waldmann, N. (2020). Source to Sink Reconstruction of a Holocene Fjord-infill: depositional patterns, suspended sediment yields, wind-induced circulation patterns and trapping efficiency for Lake Strynevatnet, inner Nordfjord, Norway. *Deposit. Record* 6, 471–485. doi: 10.1002/dep2.101

Svensen, H. (2009). *The End is Nigh: A History of Natural Disasters*. London: Reaktion Books.

Tanikawa, H., Managi, S., and Lwin, C. M. (2014). Estimates of lost material stock of buildings and roads due to the Great East Japan Earthquake and tsunami. *J. Industr. Ecol.* 18, 421–431. doi: 10.1111/jiec.12126

Thorpe, S. (1998). Some dynamical effects of internal waves and the sloping sides of lakes. *Phys. Proces. Lakes Oceans* 98, 441–460. doi: 10.1029/CE054p0441

Truong, H. V. P. (2012). "Wave-propagation velocity, tsunami speed, amplitudes, dynamic water-attenuation factors," in *Proceedings of World Conference on Earthquake Engineering* (Red Hook, NY: Curran Associates, Inc.), 1–10.

Vardy, M. E., Vanneste, M., Henstock, T. J., Clare, M. A., Forsberg, C. F., and Provenzano, G. (2017). State-of-the-art remote characterization of shallow marine sediments: the road to a fully integrated solution. *Near Surf. Geophys.* 15, 387–402. doi: 10.3997/1873-0604.2017024

Vasskog, K., Nesje, A., Støren, E. N., Waldmann, N., Chapron, E., and Ariztegui, D. (2011). A Holocene record of snow-avalanche and flood activity reconstructed from a lacustrine sedimentary sequence in Oldevatnet, western Norway. *Holocene* 21, 597–614. doi: 10.1177/0959683610391316

Vasskog, K., Paasche, Ø, Nesje, A., Boyle, J. F., and Birks, H. (2012). A new approach for reconstructing glacier variability based on lake sediments recording input from more than one glacier. *Q. Res.* 77, 192–204. doi: 10.1016/j.yqres.2011.10.001

Vasskog, K., Waldmann, N., Bondevik, S., Nesje, A., Chapron, E., and Ariztegui, D. (2013). Evidence for Storegga tsunami run-up at the head of Nordfjord, western Norway. *J. Q. Sci.* 28, 391–402. doi: 10.1002/jqs.2633

Waldmann, N., Anselmetti, F. S., Ariztegui, D., Austin, J. A. Jr., Pirouz, M., Moy, C. M., et al. (2011). Holocene mass-wasting events in Lago Fagnano, Tierra del Fuego (54° S): implications for paleoseismicity of the Magallanes-Fagnano transform fault. *Basin Res.* 23, 171–190. doi: 10.1111/j.1365-2117.2010.00489.x

Ward, S. N., and Day, S. (2002). *Suboceanic landslides. Yearbook of Science and Technology*. New York, NY: McGraw-Hill, 1.

Whiteley, J., Chambers, J., Uhlemann, S., Wilkinson, P., and Kendall, J. (2019). Geophysical monitoring of moisture-induced landslides: a review. *Rev. Geophys.* 57, 106–145. doi: 10.1029/2018RG000603

Conflict of Interest: The authors declare that the research was conducted in the absence of any commercial or financial relationships that could be construed as a potential conflict of interest.